

Transient, Biocompatible Electronics and Energy Harvesters Based on ZnO

*Canan Dagdeviren, Suk-Won Hwang, Yewang Su, Stanley Kim, Huanyu Cheng, Onur Gur, Ryan Haney, Fiorenzo G. Omenetto, Yonggang Huang, and John A. Rogers**

Semiconducting oxides are of growing interest as replacements for silicon in thin film transistors for active matrix display backplanes; they are also of potential use in transparent, flexible electronics and energy harvesters. Zinc oxide (ZnO), in particular, has a favorable combination properties, including excellent transparency in the visible wavelength range,^[1] high electron mobility,^[2] and strong piezoelectric response.^[3] As a result, ZnO, in forms ranging from films to wires and rods, has been explored in sensing,^[4–6] catalysis,^[7,8] optical emission,^[9,10] piezoelectric transduction,^[11] and actuation.^[12] Previous work also suggests that ZnO is biocompatible,^[13–15] and therefore suitable for devices that integrate on or in the human body. Here we introduce classes of ZnO based electronic devices that have, as their key attribute, the ability to dissolve completely in water or biofluids. In this way, ZnO provides an alternative to silicon^[16] or organic semiconductors^[17–20] for physically transient forms of electronics

and sensors, with expanded capabilities in energy harvesting, light emission and others. The other constituent materials of the devices presented here include magnesium (Mg) for electrodes and interconnects, magnesium oxide (MgO) for the dielectrics, and films of silk fibroin for the substrate and package. Each material used here is also biocompatible, as discussed in previous reports.^[21,22,23–26] We present specific designs and fabrication schemes for ZnO thin film transistors and mechanical energy harvesters (also for use as strain gauges). Detailed studies reveal the kinetics of dissolution and the ability to use materials and design choices to control this kinetics. Combined experimental/theoretical work illustrates the key operational features of the devices.

Figure 1a and **b** provide a schematic diagram and an image of water-soluble ZnO thin film transistors (TFTs) and mechanical energy harvesters (MEHs)/ strain gauges. Sheets of silk fibroin provide substrates and, in certain cases,

C. Dagdeviren, S.-W. Hwang, S. Kim, R. Haney,
Prof. J. A. Rogers
Department of Materials Science and Engineering
University of Illinois at Urbana-Champaign
Urbana, Illinois 61801, USA
E-mail: jrogers@illinois.edu

C. Dagdeviren, S.-W. Hwang, S. Kim, R. Haney, Prof. J. A. Rogers
Frederick Seitz Materials Research Laboratory
University of Illinois at Urbana-Champaign
Urbana, Illinois 61801, USA

C. Dagdeviren, S.-W. Hwang, S. Kim, R. Haney, Prof. J. A. Rogers
Beckman Institute for Advanced Science and Technology
University of Illinois at Urbana-Champaign
Urbana, Illinois 61801, USA

Y. Su, H. Cheng, Prof. Y. Huang
Department of Mechanical Engineering
Northwestern University
Evanston, Illinois 60208, USA

Y. Su, H. Cheng, Prof. Y. Huang
Department of Civil and Environmental Engineering
Northwestern University
Evanston, Illinois 60208, USA

Y. Su
Center for Mechanics and Materials
Tsinghua University
Beijing 100084, China

O. Gur, Prof. J. A. Rogers
Department of Electrical and Computer Engineering
University of Illinois at Urbana-Champaign
Urbana, Illinois 61801, USA

O. Gur
William L. Everitt Laboratory
University of Illinois at Urbana-Champaign
Urbana, Illinois 61801, USA

F. G. Omenetto
Department of Biomedical Engineering
Tufts University
Medford, Massachusetts 02155, USA

F. G. Omenetto
Department of Physics
Tufts University
Medford, Massachusetts 02155, USA

Prof. J. A. Rogers
Department of Chemistry
University of Illinois at Urbana-Champaign
Urbana, Illinois 61801, USA

Prof. J. A. Rogers
Department of Mechanical Science and Engineering
University of Illinois at Urbana-Champaign
Urbana, Illinois 61801, USA



DOI: 10.1002/sml.201300146

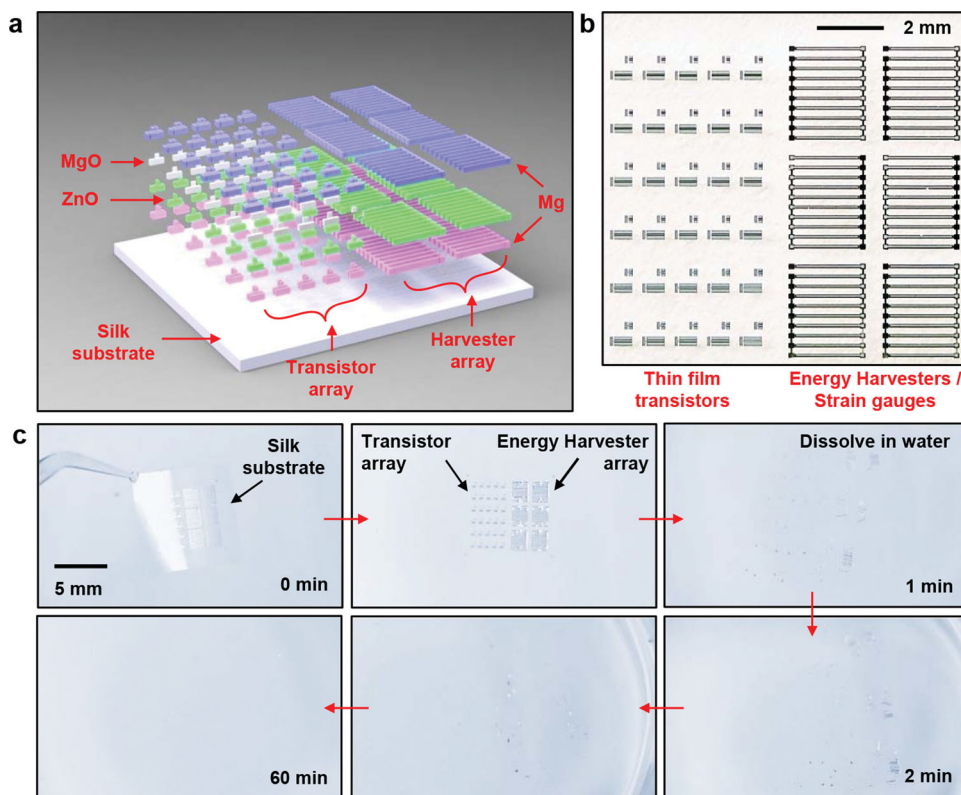


Figure 1. Materials and designs for transient thin film transistors (TFTs) and mechanical energy harvesters (MEHs)/strain gauges based on ZnO, Mg, MgO, and silk. a) Schematic illustration of transient ZnO TFTs and MEHs/strain gauges that consist entirely of water soluble materials: ZnO (semiconductor/piezoelectric), Mg (conductor), MgO (insulator), silk (substrate). b) Photograph of a collection of ZnO TFTs and MEHs on a silk substrate. All electronic materials were deposited through high-resolution shadow masks made of polyimide (PI) film (Kapton, 12.5 μm , Dupont, USA). c) A set of images of an array of ZnO TFTs and MEHs on silk, at various times after immersion in deionized water at room temperature.

encapsulating layers. Magnesium, deposited by electron beam evaporation through fine-line stencil masks made of polyimide (PI) films (Kapton, 12.5 μm , Dupont, USA), is used for the electrodes and interconnects (thicknesses between 200 and 500 nm). A first layer of Mg defines the source/drain electrodes for the TFTs (and, therefore the channel length, L_{ch}) and the bottom electrodes of the MEHs. Sputter deposition of thin films of ZnO (thicknesses between 350 and 500 nm) through PI masks forms semiconducting and piezoelectric components of the devices. The widths of the patterned ZnO films determine the channel widths (W) of the transistors. Layers of MgO (thicknesses between 100 and 150 nm) deposited by electron beam evaporation through PI masks serve as the gate dielectric layers for the TFTs. An additional patterned deposition of Mg (~400 nm) yields top electrodes for MEHs, and source, drain and gate contacts for the TFTs. A top encapsulating layer of silk can be applied by spin casting. All constituent materials, i.e. Mg (electrodes, contacts and interconnects), MgO (gate and interlayer dielectrics), ZnO (active material for the TFTs and energy harvesters/strain gauges) and silk (substrate and encapsulant), dissolve in water. The products of this dissolution include $\text{Mg}(\text{OH})_2$, $\text{Si}(\text{OH})_4$ and $\text{Zn}(\text{OH})_2$. Previous studies suggest that these compounds, and the device materials themselves, are biocompatible and environmentally benign.^[14,27,28] Figure 1c includes a set of images collected in a time sequence during dissolution in deionized

water (DI) at room temperature. The silk substrate (~25 μm), in the formulation used for this example, quickly disappears by simple dissolution. This process causes the device structures to physically disintegrate. Afterward, each remaining material disappears due to hydrolysis at different rates, as described in the following sections and previous reports.^[29–33] The time frames for dissolution can be programmed not only by encapsulation and packaging methods, but also by choices of dimensions, thicknesses and configurations in the materials for the device structures.

Dissolution of the constituent materials, other than the silk, involves hydrolysis to produce metal hydroxides. In the case of ZnO, the product is zinc hydroxide ($\text{Zn}(\text{OH})_2$), as a result of the reaction $\text{ZnO} + \text{H}_2\text{O} \leftrightarrow \text{Zn}(\text{OH})_2$. Figure 2a shows a collection of images of a meander trace of ZnO (200 nm) at various times during hydrolysis. The trace completely disappears after 15 hours, in DI water at room temperature. The mechanisms of dissolution of ZnO can be analytically described by reactive diffusion models, in which water diffusion into the materials is the rate limiting process. Previous reports describe in detail the dissolution behaviors of ZnO and the dependence on pH, temperature, dimensions and surface structures.^[27,34–37] Additional experiments on dissolution, monitored by measurements of thickness as a function of time during immersion in several different types of solutions, such as phosphate buffer saline (PBS, pH 4.0, Sigma-

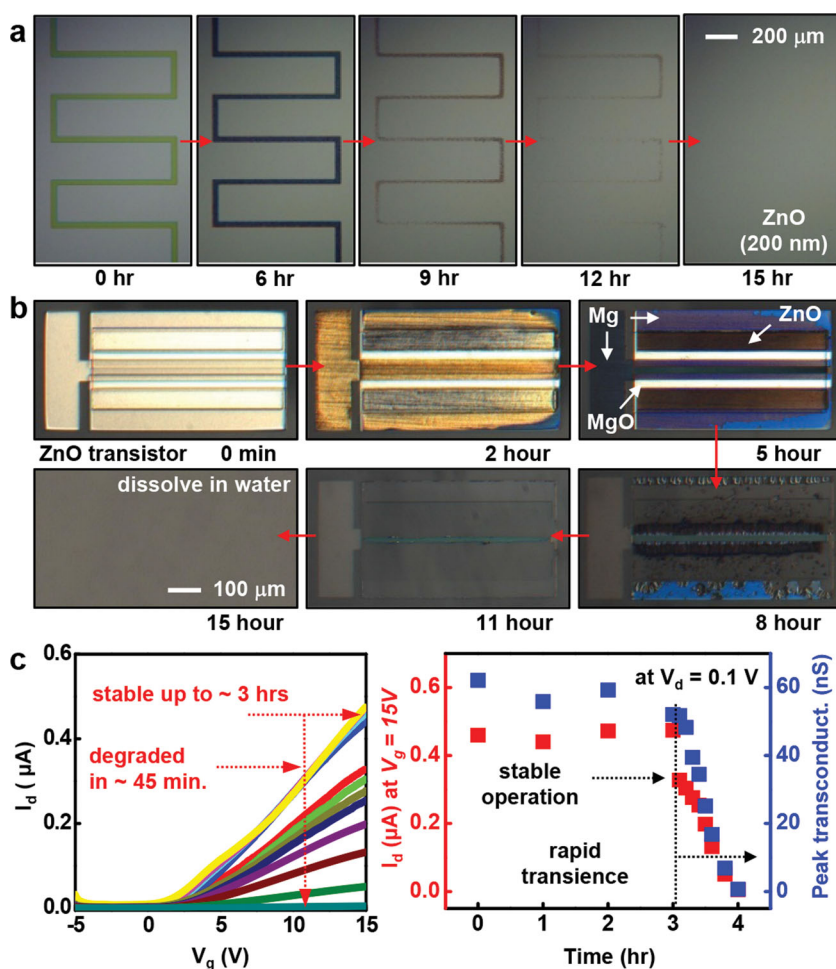


Figure 2. Dissolution kinetics of water soluble electronic materials, and devices. a) A series of optical microscope images collected at various times during dissolution of a meander trace of ZnO (200 nm) immersed in deionized water at room temperature. b) Images of a representative ZnO TFT at various times during dissolution. All components fully dissolve. c) Experimental results of degradation in electrical properties of a ZnO TFT encapsulated with MgO (500 nm) at various times after immersion in DI water. The linear scale transfer curves (left) and the drain current (I_d) at drain and gate voltages of $V_d = 0.1$ V and $V_g = 5$ V, respectively, and the peak transconductance (right) show that the operation of the device is stable for ~ 3 h, after which the properties quickly degrade in ~ 45 min.

Aldrich, USA) serum, and comparison of the results with theoretical models (see SI for details) appear in Figure S1a. The rate of dissolution ZnO increases with decreasing pH, consistent with a previous literature report.^[27] In acidic solution, the dissolution of ZnO is also attributed to the reaction, $\text{ZnO} + 2\text{H}^+ \rightarrow \text{Zn}^{2+} + \text{H}_2\text{O}$. A set of optical micrographs shows a fully formed ZnO TFT undergoing dissolution under similar conditions, as presented in Figure 2b. All electronic materials, i.e. Mg, MgO and ZnO, completely dissolve in 15 h after immersion in DI water at room temperature, in a controlled manner, without cracking, flaking or delamination. For the device dimensions studied here, the thicknesses of the layers determine, in large part, the timescales for dissolution.

Figure 2c summarizes the temporal variation in the electrical properties of a ZnO TFT, as it dissolves. (See Figure S1b for an image and diagram of the device.) In this case, a plate of glass serves as the substrate, and a layer of MgO (500 nm), deposited by electron beam evaporation, encapsulates

the entire system everywhere except at the contacts for source, drain, and gate electrodes which themselves are not immersed. Measured transfer curves, drain currents (I_d) and peak transconductances show stable operation for ~ 3 h, followed by rapid degradation over the next ~ 45 min. (Additional electrical properties appear in Figure S1c.) The encapsulant and the device materials (mainly the Mg in this case) define the first and second timescales, respectively. The results of Figure 2c are only representative. The encapsulant material and thickness can be selected to achieve stable periods of device operation that match requirements for specific applications. For example, silk can be combined with MgO to enable the lifetime to extend from minutes to years, as demonstrated in a previous result.^[16] Complete electrical and mechanical characterization of ZnO TFTs and MEHs appear in Figure 3. All electrical measurements and bending studies were performed in a dry environment. Here, the TFTs use Mg (150 nm, source, drain and gate electrodes), ZnO (200 nm, active layer), MgO (100 nm, gate dielectric). Figure 3b illustrates additional details in optical micrographs of a typical TFT, collected after defining the channel configuration (top) and completing the fabrication (bottom). Analysis of current-voltage (I - V) characteristics (Figure 3c,d) of a typical device (channel length (L_{ch}) and width (W) are 20 μm and 500 μm , respectively) yields a mobility of ~ 0.95 $\text{cm}^2/\text{V}\cdot\text{s}$, an on/off ratio of $>10^3$, a subthreshold swing of ~ 1 V/dec (at $V_d = 0.1$ V) and a threshold voltage of ~ 1 V. (See details on contact resistance of Mg

in Figure S1d). These properties are similar to those of non-transient counterparts.^[38–41] Previous literature studies suggest that deposition procedures and subsequent processing conditions for ZnO strongly affect the electrical properties.^[38,42–45] Careful parametric studies reveal conditions for sputter deposition that yield transistor characteristics (i.e. mobilities, on/off ratios, etc) in transient devices on silk that fall into a well established range set by more conventional sets of materials and substrates.^[40,46]

Figure 3e presents an image of an array of MEHs, each with a capacitor type geometry. A layer of ZnO (500 nm) lies between bottom (300 nm) and top electrodes (500 nm) of Mg that define an active area of 50 $\mu\text{m} \times 2$ mm. An MEH consists of six groups of devices; each group includes ten separate capacitor structures electrically connected in parallel. The six groups are connected in series. A IPC Flexural Endurance Tester (Model: CK-700FET) enables accurate evaluation of properties under bending. The test configuration involves the

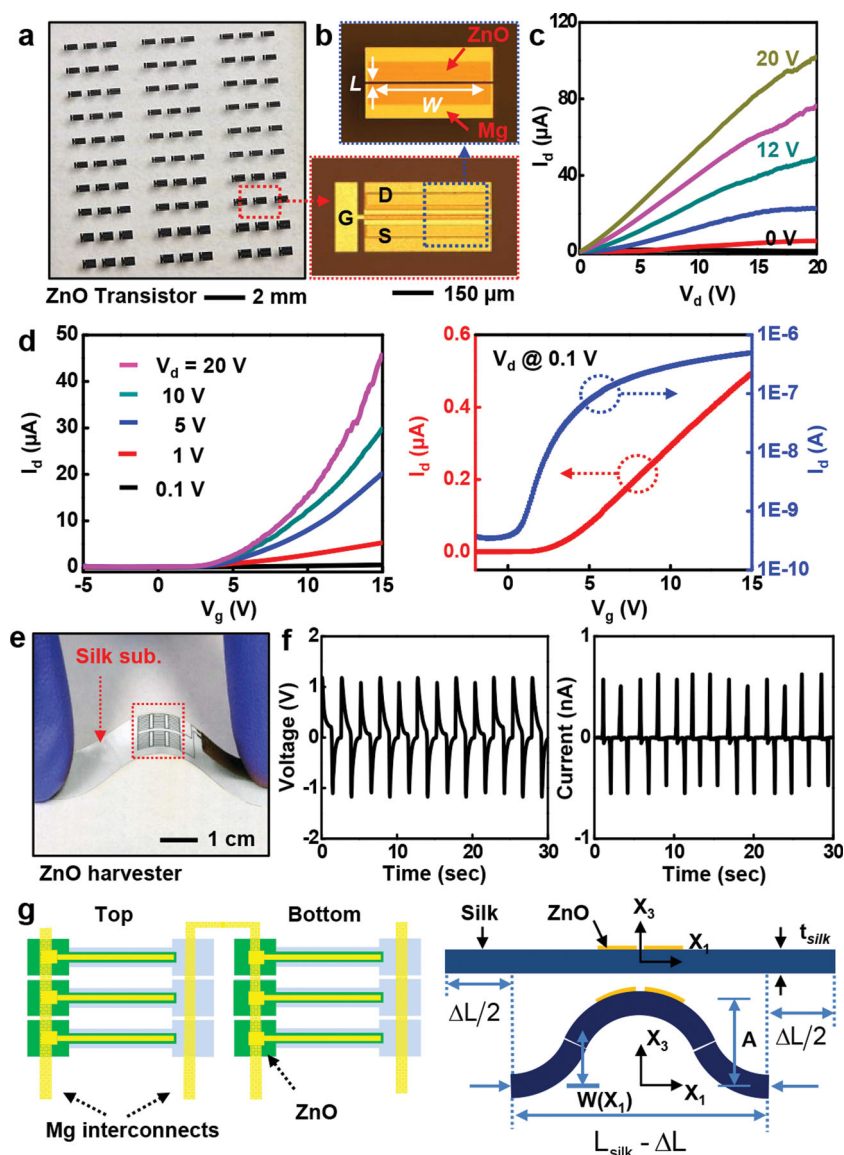


Figure 3. Electrical characterization of ZnO TFTs and MEHs. a) Image of an array of ZnO TFTs on a silk substrate. The devices use Mg (source, drain, and gate electrodes), ZnO (active layer) and MgO (gate dielectric). b) Optical micrographs of a TFT, after defining the channel configuration (top), and after completing the fabrication (bottom). c) Current-voltage characteristics of a typical device, at different gate biases. d) Linear scale transfer curves at various drain voltages (left), and linear (red) and log scale (blue) transfer curves at a drain voltage of 0.1 V (right). e) Optical micrograph of a transient, ZnO energy harvester on a thin film silk substrate, in a bent configuration. f) Output voltage vs time and output current vs time during cycles of bending. g) Schematic illustration of ZnO strips connected in series, and the theoretical shape for buckling of a device under compression.

two edges of the sample fixed within the two sliding fixtures of the instrument. During compression, the sample mechanically buckles upward to generate a well-defined, although non-uniform bending moment. Periodic variations in positive and negative voltage output peaks accompany the application and release of the buckling stresses (tensile at the location of the devices), respectively. The voltage and current outputs from an MEH are ~ 1.14 V and ~ 0.55 nA, as shown in Figure 3f. The peak output power density is ~ 10 nW/cm². The output averaged over the entire range of deformation, combined with a theoretical analysis of the mechanical input

power required to bend the device, suggests a conversion efficiency of 0.28%, but in a way that is dependent on many parameters of the system, including the external electrical load. See Supporting Information. The structures are not fully optimized for efficiency. High absolute efficiencies might not be a relevant goal for many applications in bio-integrated devices. In such cases, the aim is to collect enough power to operate a device (e.g. a pacemaker), but to do so without inducing significant mechanical loading on natural motions of the relevant part of the body. High efficiency operation would, necessarily, impose constraints on motion, due to conversion of a significant fraction of mechanical work into electrical power. Such constraints can have adverse biological consequences, particularly in an organ like the heart which responds to mechanical loading by arrhythmic behavior. The efficiency can be improved through optimized choices of thicknesses, lengths, widths and Young's moduli for the substrate and piezoelectric layers.^[47] Furthermore, reduction in viscoelastic dissipation of the substrate can be beneficial.^[42] Figure 3g gives a schematic illustration of narrow strips of ZnO films connected in series, and the theoretically predicted shape of the buckled device.

Analytical models that couple the mechanical deformation and the piezoelectric effect provide additional insights into the behaviours. Compression of the silk substrate of length L_{silk} leads to its buckling with a representative out-of-plane displacement $w = A[1 + \cos(2\pi x_1/L_{\text{silk}})]/2$, where the origin of coordinate x_1 is at the center of silk substrate, and the amplitude A is related to the compression ΔL between two ends of the silk substrate by $A \approx (2/\pi)\sqrt{L_{\text{silk}} \cdot \Delta L}$ (see SI for details). The ZnO strips, together with the top and bottom electrodes, bend with the buckled silk substrate. The strain in the ZnO consists of membrane and bending strains. The membrane strain is given analytically by $\varepsilon_m = 4\pi\sqrt{\Delta L/L_{\text{silk}}}(EI_{\text{silk}}/EI_{\text{comp}})(h/L_{\text{silk}})$ ^[48] (see SI for details), where EI_{silk} and EI_{comp} are the bending stiffnesses of the silk substrate and the composite structure of ZnO strips with electrodes and silk substrate, respectively; and h is the distance between the center of ZnO strips and the neutral mechanical plane of the composite structure (Figure S2). The bending strain is much smaller than the membrane strain since the ZnO strips are very thin. As a result, the total strain is essentially the same with the membrane strain. In addition, the bending strain has opposite signs above and below the center

of ZnO strips and does not contribute to the voltage and current output of the MEH (see SI for details).

The ZnO strips are transversely isotropic with elastic, piezoelectric, and dielectric constants c_{ij} , e_{ij} , and k_{ij} , respectively. The polarization direction x_3 is normal to the surface of the strip and the surface of the silk substrate. For plane-strain deformation ($\epsilon_{22} = 0$) the strain ϵ_{33} and the electric field E_3 along the polarization direction x_3 satisfy the constitutive relations $0 = c_{13}\epsilon_{11} + c_{33}\epsilon_{33} - e_{31}E_3$ and $D_3 = e_{31}\epsilon_{11} + e_{33}\epsilon_{33} + k_{33}E_3$, where the electric displacement D_3 along the polarization direction is a constant to be determined. For measurements of current, the top and bottom electrodes are connected to an ammeter as shown in Figure S2b. The ammeter has negligible electrical resistance, and therefore negligible voltage drop. The current (through the electrodes and ammeter) results from the moving charge induced by the strain in the ZnO (i.e., piezoelectric effect) even without voltage between the top and bottom electrodes. The zero voltage between the top and bottom electrodes of each ZnO strip, together with the above equations, gives $D_3 = \bar{e}\epsilon_m$ $\bar{e} = e_{31} - (c_{13}/c_{33})e_{33}$, where \bar{e} is the effective piezoelectric constant. For each group of device in series, the current is given by $I = -A_{ZnO}\dot{D}_3$, where A_{ZnO} is total area of ZnO strips in each group. For a representative compression $\Delta L = \Delta L_{max}[1 - \cos(2\pi t/T)]^2/4$ with the maximum compression ΔL_{max} and period T , the maximum current is obtained as

$$I_{max} = 4\pi^2 \frac{(-\bar{e}) A_{ZnO}}{T} \frac{\bar{E} I_{silk} h}{\bar{E} I_{comp} L_{silk}} \sqrt{\frac{\Delta L_{max}}{L_{silk}}} \quad (1)$$

For $\Delta L_{max} = 1.5$ cm, $T = 2.3$ second and $L_{silk} = 3$ cm as in experiments, $\bar{E} I_{silk} / \bar{E} I_{comp} = 0.34$, $h = 5.5$ μm and $A_{ZnO} = 1.08$ mm^2 from the specimen geometry (see SI for details), and $\bar{e} = -0.67$ C/m², which is on the same order of magnitude as the literature values.^[8,49] Equation (1) gives the maximum current $I_{max} = 0.55$ nA, which agrees well with the experimental result as shown in Figure 3f.

For measurements of voltage, if V denotes the total voltage for n groups of devices in series, then the voltage across each group is V/n . The electric displacement becomes $D_3 = \bar{e}\epsilon_m + \bar{k}V/(nt_{ZnO})$, where $\bar{k} = k_{33} + (e_{33}^2/c_{33})$ is the effective dielectric constant and t_{ZnO} is the thickness of ZnO strips. The current $I = -A_{ZnO}\dot{D}_3$ is also related to the voltage V and resistance R of the voltmeter by $I = V/R$, which gives $V/R = -A_{ZnO}\dot{D}_3$, or equivalently

$$\frac{dV}{dt} + \frac{nt_{ZnO}}{A_{ZnO}R\bar{k}}V = -\frac{n\bar{e}t_{ZnO}}{\bar{k}} \frac{d\epsilon_m}{dt} \quad (2)$$

For $\Delta L = \Delta L_{max}[1 - \cos(2\pi t/T)]^2/4$ and the initial condition $V(t=0) = 0$, the maximum voltage is given by

$$V_{max} \approx 4\pi^2 R \frac{(-\bar{e}) A_{ZnO}}{T} \frac{\bar{E} I_{silk} h}{\bar{E} I_{comp} L_{silk}} \sqrt{\frac{\Delta L_{max}}{L_{silk}}} \quad (3)$$

For $R = 2.3 \times 10^9$ Ω in the experiment, the theory gives the maximum voltage 1.1V, which agrees well with experiment result of 1.14V. In addition to electrical characterization of devices, the intrinsic piezoelectric and morphological properties of active layer ZnO thin film by sputtering system

was studied by AFM, SEM, and XRD techniques in detail (Figure S3).

The results presented here indicate that ZnO can be used effectively as an active material for transient electronics, as well as for energy harvesting and strain sensing devices, for which all of the constituent elements dissolve completely in water. Compared to silicon, ZnO has features, such as wide, direct bandgap and piezoelectric responses, that could enable expanded capabilities in transient devices. The use of this material alone, or in heterogeneous configurations with silicon, opens up additional application possibilities for transient technologies, in areas ranging from biomedicine, to environmental monitoring and certain areas of consumer electronics.

Experimental Section

Fabrication of ZnO TFTs and MEHs: All electronic materials were directly deposited onto silk substrates through high resolution stencil masks made of polyimide (PI) films (Kapton, 12.5 μm , Dupont, USA). These materials consist of ZnO (semiconductor), Mg (conductors), MgO (insulators), and silk (substrate). A layer of Mg (150 nm) deposited by electron beam evaporation (Temescal) defined the source and drain electrodes for the TFTs. ZnO (200 nm) deposited by RF magnetron sputtering (AJA) through a PI mask served as the semiconductor. A high-purity of ZnO target was used (99.99%), with base pressures of 2×10^{-6} torr, and working pressures of 15 mTorr, maintained with a Ar (99.99%):O₂ = 2:1 (sccm) gas mixture. The sputtering was performed at room temperature (RT) with an RF power of 250 W, immediately after cleaning the target with Ar plasma for 5 min. The deposition rate was ~ 150 nm/h. Electron beam evaporation of MgO (100 nm), also through PI masks, defined the gate dielectrics. The gate electrode consisted of Mg (300 nm), deposited and patterned using schemes similar to those for the source and drain.

ZnO MEHs were designed in six groups, each of which contains ten separate devices (ZnO strips with Mg electrodes on top and bottom, in a capacitor type geometry). Devices within each group were connected in parallel; the six groups themselves were connected in series. The fabrication began with deposition of Mg (300 nm) by electron beam evaporation through a PI shadow mask, to form bottom electrodes. A layer of ZnO (400–500 nm) was then formed by RF sputtering, through a shadow mask aligned to the Mg bottom electrodes. Top electrodes of Mg (~ 500 nm) were formed in a manner similar to that for the bottom electrodes. Individual ZnO strips defined active areas of $50 \mu\text{m} \times 2$ mm. Square pads at their ends facilitated electrical top and bottom contacts. The ZnO layer was formed in a geometry slightly bigger than that of the bottom electrode to avoid shorting of top to bottom, as seen in Figure S2.

Investigation of ZnO Thin-Film Properties and Device Analysis: X-ray diffraction (XRD, Philips X'pert) revealed that the films consist of hexagonal ZnO, with preferred orientation of (002). Scanning electron microscope (SEM, Hitachi S4800) imaging determined the surface topography and provided cross sectional views of the films. Measurements of voltage induced displacements in thin films of ZnO were conducted by atomic force microscopy (AFM, Asylum Cypher, USA). A semiconductor parameter analyzer (4155C, Agilent) was used to measure the electrical characteristics of TFTs and MEHs.

Bending Tests for Energy Harvesters/Strain Gauges: A commercial instrument (IPC Flexural Endurance Tester Model: CK-700FET) was used to perform bending experiments. The test involved compressing a sheet of devices between two clamped edges; the result was a buckling structure whose curvature was defined by the extent of compression. Electrical measurements revealed positive and negative swings in voltage and current output, corresponding to the application and release of such buckling stresses. An analytical model of the mechanical deformations and the associated piezoelectric effects captured the experimental observations.

Dissolution Experiments: Dissolution tests were performed to study degradation behaviors of devices and kinetics of materials removal. To observe dissolution of ZnO, a meander trace of ZnO (200 nm) on a glass substrate was submerged in DI water at room temperature. Optically significant changes were observed after 9 hours, and complete disappearance occurred in 15 h. In a similar way, a ZnO transistor, consisting of Mg, MgO, and ZnO, on glass was used to illustrate the various stages of dissolution at the device level. Most components disappeared within 8 h; complete dissolution occurred within 15 h. In addition, measurements of changes in electrical properties defined timescales of device function. A transistor with a design similar to that described above was prepared and encapsulated with a layer of MgO (500 nm). Measured and calculated characteristics revealed two-stage kinetics. The first was determined by the encapsulation layer; the second, primarily by the Mg electrodes.

Supporting Information

Supporting Information is available from the Wiley Online Library or from the author.

Acknowledgements

C. Dagdeviren and S.-W. Hwang contributed equally to this work. This material is based upon work supported by the Defense Advanced Research Projects Agency. Anoop Damodaran is acknowledged for support during PFM test.

- [1] S. Mondal, K. P. Kanta, P. Mitra, *J. Phys. Sci.* **2008**, *12*, 221.
- [2] K. Miyamoto, M. Sano, H. Kato, T. Yao, *J. Cryst. Growth* **2004**, *265*, 34.
- [3] M. H. Zhao, Z. L. Wang, S. X. Mao, *Nano Lett.* **2004**, *4*, 587.
- [4] S. K. Gupta, A. Joshi, M. Kaur, *J. Chem. Sci.* **2010**, *122*, 57.
- [5] N. Kumar, A. Dorfman, J. I. Hahm, *Nanotechnology* **2006**, *17*, 2875.
- [6] H. Gullapalli, V. S. M. Vemuru, A. Kumar, A. Botello-Mendez, R. Vajtai, M. Terrones, S. Nagarajiah, P. M. Ajayan, *Small* **2010**, *6*, 1641.
- [7] L. Saad, M. Riad, *J. Serb. Chem. Soc.* **2008**, *73*, 997.
- [8] B. V. Kumar, H. S. B. Naik, D. Girija, B. V. Kumar, *J. Chem. Sci.* **2011**, *123*, 615.
- [9] S. Baskoutas, G. Bester, *J. Phys. Chem. C* **2011**, *115*, 15862.
- [10] C. Czekalla, J. Guinard, C. Hanisch, B. Q. Cao, E. M. Kaidashev, N. Boukos, A. Travlos, J. Renard, B. Gayral, D. L. S. Dang, M. Lorenz, M. Grundmann, *Nanotechnology* **2008**, *19*, 115202.
- [11] H. Choi-Yim, R. Busch, W. L. Johnson, *J. Appl. Phys.* **1998**, *83*, 7993.
- [12] F. R. Blom, D. J. Yntema, F. C. M. Van De Pol, M. Elwenspoek, J. H. J. Fluitman, T. J. A. Popma, *Sens. Actuat.* **1990**, *21*, 226.
- [13] Z. Li, R. Yang, M. Yu, F. Bai, C. Li, Z. L. Wang, *J. Phys. Chem. C* **2008**, *112*, 20114.
- [14] Y. F. Zheng, R. Z. Li, Y. D. Wang, *Int. J. Modern Phys. B* **2009**, *23*, 1566.
- [15] S. Dutta, S. Basak, P. K. Samanta, *Int. J. Nanosci. Nanotechnol.* **2012**, *3*, 27.
- [16] S. W. Hwang, H. Tao, D. H. Kim, H. Cheng, J. K. Song, E. Rill, M. A. Brenckle, B. Panilaitis, S. M. Won, Y. S. Kim, Y. M. Song, K. J. Yu, A. Ameen, R. Li, Y. Su, M. Yang, D. L. Kaplan, M. R. Zakin, M. J. Slepian, Y. Huang, F. G. Omenetto, J. A. Rogers, *Science* **2012**, *337*, 1640.
- [17] C. Legnani, C. Vilani, V. L. Calil, H. S. Barud, W. G. Quirino, C. A. Achete, S. J. L. Ribeiro, M. Cremona, *Thin Solid Films* **2008**, *517*, 1016.
- [18] M. Irimia-Vladu, P. A. Troshi, M. Reisinger, L. Shmygleva, Y. Kanbur, G. Schwabegger, M. Bodea, R. Schwödäuer, A. Mummyatov, J. W. Fergus, V. F. Razumov, H. Sitter, N. S. Sariciftci, S. Bauer, *Adv. Funct. Mater.* **2010**, *20*, 4069.
- [19] C. J. Bettinger, Z. Bao, *Polym. Int.* **2010**, *59*, 563.
- [20] C. J. Bettinger, Z. Bao, *Adv. Mater.* **2010**, *22*, 651.
- [21] B. Panilaitis, G. H. Altman, J. Chen, H. J. Jin, V. Karageorgiou, D. L. Kaplan, *Biomaterials* **2003**, *24*, 3079.
- [22] M. Moravej, D. Mantovani, *Int. J. Mol. Sci.* **2011**, *12*, 4250.
- [23] S. P. Hudson, R. F. Padera, R. Langer, D. S. Kohane, *Biomaterials* **2008**, *29*, 4045.
- [24] B. G. Trewyn, J. A. Nieweg, Y. Zhao, V. S. Y. Lin, *Chem. Engin. J.* **2008**, *137*, 23.
- [25] S. Shen, P. S. Chow, F. Chen, R. B. Tan, *Chem. Pharm. Bull.* **2007**, *55*, 985.
- [26] C. Martinez-Boubeta, L. Balcells, R. Cristófol, C. Sanfeliu, E. Rodríguez, R. Weissleder, S. Lope-Piedrafita, K. Simeonidis, M. Angelakeris, F. Sandiumenge, A. Calleja, L. Casas, C. Monty, B. Martínez, *Nanomed. Nanotechnol. Biol. Med.* **2010**, *6*, 362.
- [27] J. Zhou, N. Xu, Z. L. Wang, *Adv. Mater.* **2006**, *18*, 2432.
- [28] I. Shimizu, D. MacFarlane, *Dermatol. Surgery* **2012**, *38*, 965.
- [29] M. H. Grosjean, L. Roué, *J. Alloys Compounds* **2006**, *416*, 296.
- [30] D. J. Wales, J. P. K. Doye, *J. Chem. Phys.* **2003**, *119*, 12409.
- [31] K. Wegner, H. C. Lya, R. J. Weissa, S. E. Pratsinisa, A. Steinfeld, *Int. J. Hydrogen Energy* **2006**, *31*, 55.
- [32] R. B. Reed, D. A. Ladner, C. P. Higgings, P. Westerhoff, J. F. Ranville, *Environ. Toxicol. Chem.* **2012**, *31*, 93.
- [33] G. Song, A. Atrens, *Adv. Engin. Mater.* **2003**, *5*, 837.
- [34] M. Valtiner, S. Borodin, G. Grundmeier, *Langmuir* **2008**, *24*, 5350.
- [35] C. David, J. Galceran, C. Rey-Castro, J. Puy, E. Companys, J. Salvador, J. Monne, R. Wallace, A. Vakourov, *J. Phys. Chem.* **2012**, *116*, 11758.
- [36] H. Gerischer, N. Sorg, *Electrochim. Acta* **1992**, *37*, 827.
- [37] A. Mudunkotuwa, T. Rupasinghe, C. Wu, V. Grassian, *Langmuir* **2012**, *28*, 396.
- [38] H. Jeon, K. Noh, D. Kim, M. Jeon, *J. Korean Phys. Soc.* **2007**, *51*, 1999.
- [39] X. Zhang, J. Zhang, W. Zhang, X. Hou, *J. Mater. Sci. Mater. Electron.* **2010**, *21*, 671.
- [40] R. Hoffman, B. Norris, J. Wagera, *Appl. Phys. Lett.* **2003**, *82*, 733.
- [41] P. F. Garcia, R. S. McLean, M. H. Reilly, *Appl. Phys. Lett.* **2006**, *88*, 123509.
- [42] C. Chang, V. H. Tran, J. Wang, Y. K. Fuh, L. Lin, *Nano Lett.* **2010**, *10*, 726.
- [43] G. B. Stringfellow, *Organometallic Vapor-Phase Epitaxy: Theory and Practice*, Academic, San Diego **1998**, p.4.
- [44] S. Masuda, K. Kitamura, Y. Okumura, S. Miyatake, H. Tabata, T. Kawai, *J. Appl. Phys.* **2003**, *93*, 1624.

- [45] J. M. Camacho, R. Castro-Rodríguez, A. Iribarren, E. Chan y Díaz, A. Duarte-Moller, P. Sánchez Santiago, *Int. J. Phys. Sci.* **2011**, *6*, 6660.
- [46] C. J. Park, Y. W. Kim, Y. J. Cho, S. M. Bobade, D. K. Choi, S. B. Lee, *J. Korean Phys. Soc.* **2009**, *55*, 1925.
- [47] Q. M. Wang, X. H. Du, B. Xu, L. E. Cross, *Ultrasonics Ferroelec. Frequency Control. IEEE Trans.* **1999**, *46*, 638.
- [48] S.-I. Park, J.-H. Ahn, X. Feng, S. Wang, Y. Huang, J. A. Rogers, *Adv. Funct. Mater.* **2008**, *18*, 2673.
- [49] F. Bernardini, V. Fiorentini, D. Vanderbilt, *Phys. Rev. B* **1997**, *56*, 10024.

Received: January 15, 2013
Published online: April 19, 2013